Persistent junk solutions in time-domain modeling of extreme mass ratio binaries

Scott E. Field,[1,*] Jan S. Hesthaven,[2,†] and Stephen R. Lau[3,‡]

[1]*Department of Physics, Brown University, Providence, Rhode Island 02912, USA*
[2]*Division of Applied Mathematics, Brown University, Providence, Rhode Island 02912, USA*
[3]*Mathematics and Statistics, University of New Mexico, Albuquerque, New Mexico 87131, USA*

In the context of metric perturbation theory for nonspinning black holes, extreme mass ratio binary systems are described by distributionally forced master wave equations. Numerical solution of a master wave equation as an initial boundary value problem requires initial data. However, because the correct initial data for generic-orbit systems is unknown, specification of trivial initial data is a common choice, despite being inconsistent and resulting in a solution which is initially discontinuous in time. As is well known, this choice leads to a burst of junk radiation which eventually propagates off the computational domain. We observe another potential consequence of trivial initial data: development of a persistent spurious solution, here referred to as the *Jost junk solution*, which contaminates the physical solution for long times. This work studies the influence of both types of junk on metric perturbations, waveforms, and self-force measurements, and it demonstrates that smooth modified source terms mollify the Jost solution and reduce junk radiation. Our concluding section discusses the applicability of these observations to other numerical schemes and techniques used to solve distributionally forced master wave equations.

I. INTRODUCTION

Extreme mass ratio binary (EMRB) systems are typically comprised of a small compact object, such as a stellar black hole, orbiting a supermassive blackhole, and the gravitational radiation generated by such systems is potentially detectable by the LISA project. A number of approaches attempt to model the resulting gravitational waveforms, including effective one-body formulations [1–3], effective field theory techniques [4,5], post-Newtonian expansions [6], self-force effects [7–10], and different gauge choices [11–13]. When including high-order effects or performing comparisons between techniques, improved EMRB modeling will increasingly require the identification and reduction of all error sources (both numerical and systematic).

Consider a small perturbation $h_{\mu\nu}$ of a fixed background Schwarzschild metric, where $h_{\mu\nu}$ satisfies the linearized Einstein equations. The metric perturbation $h_{\mu\nu}$ describing an EMRB can be reconstructed from a collection of scalar *master functions* Ψ, each of which obeys a forced wave equation of the form (with all multipole indices suppressed)

$$-\partial_t^2\Psi + \partial_x^2\Psi - V(r)\Psi = f(r)[G(t,r)\delta(r - r_p(t))$$
$$+ F(t,r)\delta'(r - r_p(t))]. \quad (1)$$

The coordinates here are the areal radius r, the Regge-Wheeler tortoise coordinate $x = r + 2M\log(\frac{1}{2}r/M - 1)$,

and the time-dependent radial location $r_p(t)$ of the smaller mass or "particle." M is the mass parameter of the background solution, $f(r) = 1 - 2M/r$, and $V(r)$ is either the Regge-Wheeler or Zerilli potential (explicit expressions for both are given in Sec. II B). The *distributional* inhomogeneity on the right-hand side of (1) involves Dirac delta functions, as well as the ordinary functions $F(t,r)$ and $G(t,r)$. For all possible choices of the master function, $F(t,r)$ and $G(t,r)$ are listed, for example, in Refs. [14,15]. Here it suffices to note that their evaluation requires knowledge of the particle's four-velocity u^α, orbital energy and angular momentum parameters (E_p, L_p), and equatorial location $(r_p(t), \pi/2, \phi_p(t))$. In the model we study, integration of the geodesic equations determines the timelike particle trajectory $(r_p(t), \phi_p(t))$ in the equatorial plane $\theta = \pi/2$ [14,16–18].

One approach for computing EMRB waveforms is to numerically solve Eq. (1) as a time-domain initial value problem with prescribed initial data. The exact initial data for generic point-particle trajectories is nontrivial, and the most common choice is therefore to set both Ψ and its time derivative to zero. (See Refs. [19–22] for the construction of more realistic data.) Inspection of (1) shows that trivial data is inconsistent with the jump conditions stemming from the delta function terms in the inhomogeneity. As a result, trivial data results in an impulsive (i.e., discontinuous in time) start-up. This paper addresses the main question of if, and when, a *physical* solution eventually emerges from such trivial initial data. Ideally, we would have both the correct source terms and initial conditions. Without the exact initial data, we consider modifying the source terms such that they are consistent with the choice of trivial initial data. Precisely, the source terms are "switched

*Scott_Field@brown.edu
†Jan_Hesthaven@brown.edu
‡srlau@math.unm.edu

on'' smoothly via the following prescription:

$$F(t, r) \rightarrow F(t, r)$$
$$\times \begin{cases} \frac{1}{2}[\mathrm{erf}(\sqrt{\delta}(t - t_0 - \tau/2) + 1] & \text{for } t_0 \le t \le t_0 + \tau \\ 1 & \text{for } t > t_0 + \tau, \end{cases}$$
$$(2)$$

and the same for $G(t, r)$. Typically, the initial time $t_0 = 0$, and the time scale τ is much shorter than the final time of the run. Choosing suitable τ and δ, one achieves smooth and consistent start-up to machine precision.

To appreciate some of the issues associated with the main question above, consider a particle in a fixed circular orbit. The energy $\dot{E}_{\mathrm{GW}}$ and angular momentum $\dot{L}_{\mathrm{GW}}$ luminosities for gravitational waves are then constant in time and obey the relation $\dot{E}_{\mathrm{GW}} = \Omega \dot{L}_{\mathrm{GW}}$, where Ω is the angular velocity of the particle. However, verification of this relationship is limited by a finite computational domain, leading to an $O(r^{-1})$ error (see Ref. [23] for a recent suggestion towards overcoming this limitation). Therefore, numerical verification of $\dot{E}_{\mathrm{GW}} = \Omega \dot{L}_{\mathrm{GW}}$ is a useful diagnostic only in the distant wave-zone. In the near-zone we might also test "$\dot{E}_{\mathrm{GW}} = \Omega \dot{L}_{\mathrm{GW}}$," now constructing the luminosities with self-force quantities via (26) below; however, because Ψ is discontinuous at the particle location, self-force measurements will involve large errors unless due care is taken. For generic quasiperiodic orbits, selection of a meaningful set of diagnostics is not straightforward. In particular, we can neither infer steady-state behavior throughout the computational domain, nor claim we have a solution which solves the hypothetical "true" initial value boundary problem. These difficulties are due to the inconsistent initial conditions. That is, we are really solving a problem different from the physical one. As a partial resolution of these issues, we examine a direct test condition which is necessary to claim that a physically correct solution has been achieved everywhere in the computational domain. This is a simple self-consistency condition relating the Cunningham-Price-Moncrief (CPM) and Regge-Wheeler (RW) master functions. Violations of this relationship are necessarily due to numerical errors and/or incorrect initial conditions.

We will refer to errors seeded by the initial conditions as "junk." One type of junk either propagates off the computational domain or decays away. We collectively refer to such junk radiation, junk quasinormal ringing, and junk Price tails as *dynamical junk*. The key observation of this paper is that trivial initial conditions *may* also give rise to a static distributional junk solution Ψ_{Jost}, which we refer to as *Jost junk*. In terms of the "Schrödinger operator" $H = -\partial_x^2 + V$, a Jost solution satisfies $H\Psi_{\mathrm{Jost}}^{\pm} = \nu^2 \Psi_{\mathrm{Jost}}^{\pm}$, with $\Psi_{\mathrm{Jost}}^{\pm} \sim \exp(\pm i\nu x)$ as $x \rightarrow \infty$ [24]. In this paper, we are exclusively interested in "zero-energy" Jost solutions for which $\nu = 0$, in which case Ψ_{Jost} does not behave exponentially at infinity (see below). Therefore, in what follows

a Jost function satisfies a "zero-energy," time-independent, Schrödinger equation $(-\partial_x^2 + V)\Psi_{\mathrm{Jost}} = 0$ to the left and right of the particle, and, as it turns out, is discontinuous at the particle location. We find that Ψ_{Jost} has a non-negligible effect in the wave-zone, yet is often small enough to be buried into the $O(r^{-1})$ error associated with a waveform "read-off" in the far-field.

We will adopt trivial initial conditions throughout, but allow for modified "smoothed" source terms according to the aforementioned description (2). Our chief goal is to study the properties of the numerical solutions computed with and without smoothed source terms, especially in the context of the Jost solution. To carry out numerical simulations, we have primarily used the nodal Legendre discontinuous Galerkin method described in Ref. [15], and further details of this method will not be given here. In addition, some of our results have either been obtained or independently verified with a nodal Chebyshev method (similar to the one described in Refs. [25,26]), which also features multiple subdomains and upwinding. Our nodal Chebyshev method treats the jump discontinuities at the particle location in the same fashion as outlined in Ref. [15] for the nodal dG method. Both our dG and Chebyshev methods solve a first-order system representing (1). Namely,

$$\partial_\lambda \Psi = \beta^\xi \Phi - \Pi \tag{3a}$$
$$\partial_\lambda \Pi = \beta^\xi \partial_\xi \Pi - (\partial x/\partial \xi)^{-1} \partial_\xi [(\partial x/\partial \xi)^{-1} \Phi]$$
$$\quad + V(r)\Psi + J_1 \delta(\xi - \xi_p) \tag{3b}$$
$$\partial_\lambda \Phi = \partial_\xi(\beta^\xi \Phi) - \partial_\xi \Pi + J_2 \delta(\xi - \xi_p), \tag{3c}$$

where the time-space coordinates (λ, ξ) are adapted to the particle history (the particle location $\xi = \xi_p$ remains fixed in this system). Equation (3a) defines Π, the variable[1] $\Phi = \partial_\xi \Psi$, and Ref. [15] relates the λ–dependent jump terms $J_{1,2}$ to the sources in (1). Most of this paper considers circular orbits, for which $\lambda = t$, $\xi = x$, and the shift vector $\beta^\xi = 0$. We often refer to the variables Π and Φ below, and for circular orbits these are $-\partial_t \Psi$ and $\partial_x \Psi$, respectively. Throughout the paper, we make reference to the parameters listed in Table I.

This paper is organized as follows. Section II focuses on the Jost solution, from both empirical and analytical standpoints. Here we present analytic formulas for Jost solutions and compare them with numerical results. Section III considers several practical consequences of impulsive start-up for EMRB modeling with circular orbits: violation of the axial consistency condition, contamination of waveform luminosities, and influence on self-force measurements.

---

[1] In our approach, from all fields we explicitly remove delta function terms arising from the distributional inhomogeneity. Therefore, $\Phi = \partial_\xi \Psi$ does *not* hold in the sense of distributions. More precisely, in the case of circular orbits, our Φ is $\partial_x \Psi - [[\Psi]]\delta(x - x_p)$.

TABLE I.   Basic set of parameters for a numerical simulation. This set is not complete, but in what follows we often refer to these variables. For all our simulations $M = 1 = m_p$, where the choice $m_p = 1$ is equivalent to working with per-particle-mass perturbations Ψ/m_p.

a, b:	Endpoints of computational domain to $[a, b]$.
S_L, S_R:	Number of subdomains to left and right of particle.
N:	Number of points on each subdomain.
τ, δ:	Smoothing parameters introduced in Eq. (2).
Δt, t_F:	Timestep and final time.
$M = 1$:	Schwarzschild mass parameter.
$m_p = 1$:	Particle mass.

This section also gives a preliminary report on consequences for eccentric orbits. Concluding remarks are given in Sec. IV, where we touch upon finite-difference methods while discussing the universality of our results. Longer calculations appear in the Appendix.

II. JOST SOLUTION

To better explain the origin of the Jost junk solution, we first consider a toy model: the ordinary $1 + 1$ wave equation with distributional forcing. We then examine the Jost solution for the master wave equations, with a forcing determined by a circular orbit.

A. Forced $1 + 1$ wave equation

For a fixed velocity v obeying $|v| < 1$, we consider the model

$$-\partial_t^2 \Psi + \partial_x^2 \Psi = G(t)\delta(x - vt) + F(t)\delta'(x - vt)$$
$$G(t) = \cos t = -\mathrm{i}F(t).$$

Reference [15] has shown that

$$\Psi(t, x) = -\frac{1}{2}\sin\vartheta + \frac{1}{2}\mathrm{i}\gamma^2[v + \mathrm{sgn}(x - vt)]\cos\vartheta$$
$$\vartheta = \gamma^2(t - xv - |x - vt|) \qquad (5)$$

is an exact particular solution to (4). Here $\gamma = (1 - v^2)^{-1/2}$ is the usual relativistic factor. For this model, junk radiation propagates off the computational domain with speeds ± 1. However, when numerically solving this equation subject to (incorrect) trivial initial conditions, we observe that the numerical solution no longer converges to the particular solution. For simulations involving (4), we have used the dG method with (cf. Table I) $a = -100$, $b = 100$, $S_L = 10$, $S_R = 10$, $N = 27$, and $\Delta t = 0.01$. To compute errors relative to the exact solution, we have first interpolated onto a uniformly spaced x–grid with 5121 points. Furthermore, to better model the circular orbit scenario for EMRBs, we have taken $v = 0$.

With the exact solution used to generate initial conditions at $t = 0$, the nodal dG method exhibits spectral con-

vergence throughout the computational domain (and for all fields with the wave equation treated as a first-order system) [15]. However, with trivial initial conditions, only the corresponding numerical derivatives, $\Pi_{\text{numerical}}$ and $\Phi_{\text{numerical}}$, converge to the correct values, whereas $\Psi_{\text{numerical}}$ itself is off by a constant value on each subdomain. Let us write

$$\Psi_{\text{numerical}} = (\Psi_L + C_L)\Theta(-x) + (\Psi_R + C_R)\Theta(x), \quad (6)$$

where $\Theta(x)$ is the Heaviside function and the exact solution from (5) is

$$\Psi_L = -\frac{1}{2}\sin(t + x) - \frac{1}{2}\mathrm{i}\cos(t + x)$$
$$\Psi_R = -\frac{1}{2}\sin(t - x) + \frac{1}{2}\mathrm{i}\cos(t - x). \qquad (7)$$

We introduce the time-independent $1 + 1$ Jost junk solution

$$\Psi_{\text{Jost}} = C_L\Theta(-x) + C_R\Theta(x), \qquad (8)$$

in order to express the numerical solution as $\Psi_{\text{numerical}} = \Psi_{\text{exact}} + \Psi_{\text{Jost}}$.

We examine the dependence of $C = |C_L| + |C_R|$ on the smoothing parameters (τ, δ), defined analogously to those in (2), but here introduced to smooth our toy source term $\cos t\delta(x) + \mathrm{i}\cos t\delta'(x)$. We restrict the parameter space by first choosing τ, and then finding the smallest δ such that $\frac{1}{2}[\mathrm{erf}(\sqrt{\delta}(t - t_0 - \tau/2) + 1]$ is less than 10^{-16} when $t = 0$ and greater than $1 - 10^{-16}$ when $t = \tau$. These requirements ensure that the start-up phase is smooth to machine precision, while providing the most gradual rate at which the distributional source terms are turned-on. Figure 1 shows that the troublesome constant term is arbitrarily well suppressed by the smoothing procedure. However, we find that the value of C remains fixed when varying the time step. The final run time for each data point in the plot is $t_F = \tau + 150$. No essential difference exists between the $v = 0$ and $v \neq 0$ cases, except that for the latter
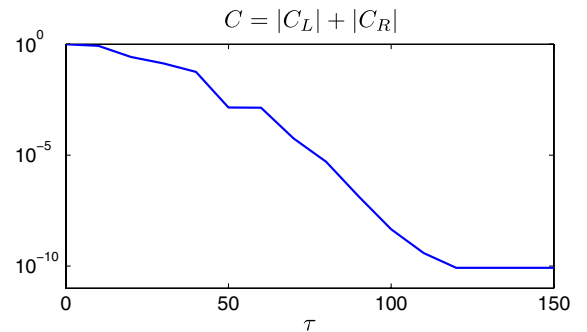

FIG. 1 (color online).   Dependence of C on smoothing parameters. We have empirically determined that $|C_L| = \frac{1}{2} = |C_R|$ for an impulsive start-up, corresponding to $C = 1$ at the leftmost point. The parameter δ is different for each τ; $\delta = 2$ for $\tau = 10$ and $\delta = 0.0058$ for $\tau = 150$.

case we must ensure that the particle does not get too close to the boundary. Let Ψ_{smooth} represent $\Psi_{\text{numerical}}$ obtained with smoothing, and $\Psi_{\text{impulsive}}$ represent $\Psi_{\text{numerical}}$ obtained without smoothing. Then we have shown $\Psi_{\text{smooth}} \simeq \Psi_{\text{exact}}$, so that

$$\Psi_{\text{Jost}} \simeq \Psi_{\text{impulsive}} - \Psi_{\text{smooth}} \tag{9}$$

is another expression for the Jost solution, valid up to method error. In the next subsection we consider this expression in the context of master wave equations.

B. Master wave equations

The first numerical experiment in this subsection involves the axial sector with

$$V^{\text{axial}}(r) = \frac{f(r)}{r^2}\left[\ell(\ell + 1) - \frac{6M}{r}\right] \tag{10}$$

in (1), and assumes CPM source terms (see the appendix of [15] for the precise expressions). To empirically verify that an impulsive start-up also leads to a Jost solution in this setting, we will form and plot the expression (9), using the Chebyshev method. Later on, we will give analytic expressions for static Jost solutions. The experiment enforces Sommerfeld boundary conditions at the left physical boundary, and radiation outer boundary conditions [15,27] on the right boundary. Our smoothing parameters are $\tau = 150$ and $\delta = 0.0058$. We compute the $(\ell, m) = (3, 2)$ metric perturbations for a particle in circular orbit initially at $(r, \phi) = (7.9456, 0)$. Other parameters (cf. Table I) are $a \simeq -202.16$, $b = 60 + 2\log(29) \simeq 66.73$, $S_L = 30$, $S_R = 8$, $N = 26$, $\Delta t \simeq 0.03$, and $t_F = 600$. Figure 2 shows the result. The plots suggest that the Jost junk solution affects $\Psi_{\text{impulsive}}^{\text{CPM}}$ and its spatial derivatives.

For both axial and polar perturbations generated by circular orbits, we now present the analytic form of the Jost solution, suppressing throughout the analysis both orbital ℓ and azimuthal m indices. For circular orbits we have observed empirically that the Jost junk solution can be written as

$$\Psi_{\text{Jost}}^{\text{axial/polar}} = C_L v_L^{\text{axial/polar}}\Theta(-x) + C_R v_R^{\text{axial/polar}}\Theta(x), \tag{11}$$

where C_L and C_R are complex constants. The functions $v_{L,R}^{\text{axial/polar}}$ satisfy a Schrödinger equation $Hv = 0$ defined by the operator

$$H^{\text{axial/polar}} = -\partial_x^2 + V^{\text{axial/polar}}, \tag{12}$$

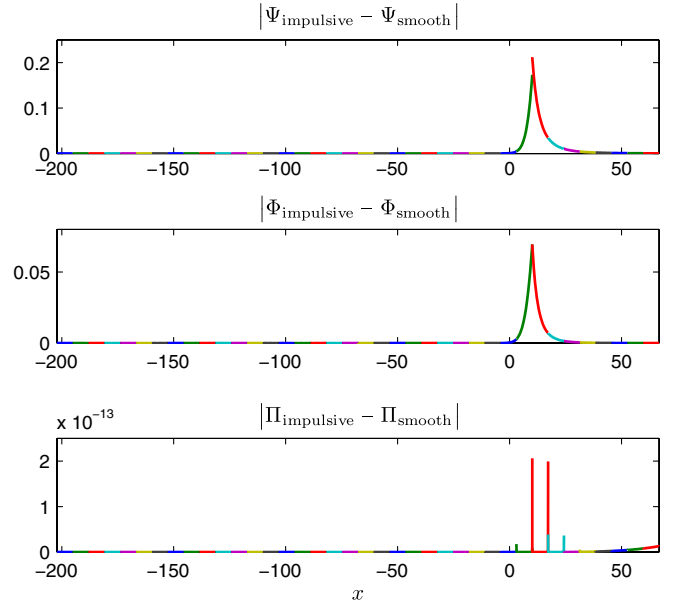where V^{axial} is given in Eq. (10) and, in terms of $n = (\ell - 1)(\ell + 2)/2$,

FIG. 2 (color online). Difference between smoothly and impulsively started CPM fields. Here $\ell = 3$, $m = 2$, and the snapshot is taken at $t = 600$.

$$V^{\text{polar}}(r) = \frac{2f(r)}{(nr + 3M)^2} \times \left[n^2\left(1 + n + \frac{3M}{r}\right) + \frac{9M^2}{r^2}\left(n + \frac{M}{r}\right)\right]. \tag{13}$$

The functions $v_L^{\text{axial/polar}}$ satisfy the Schrödinger equation to the left of the particle, and the functions $v_R^{\text{Axial/Polar}}$ the equation to the right of the particle. The relevant solutions to $Hv = 0$ decay either as $r \to 2M^+$ or $r \to \infty$.

We derive expressions for all four functions $v_{L,R}^{\text{axial/polar}}$ in the Appendix, adopting the dimensionless radius $\rho = (2M)^{-1}r$ as the basic variable. Here we record the set of axial functions,

$$v_L^{\text{axial}} = \rho^{-\ell}{}_2F_1(\ell + \jmath + 1, \ell - \jmath + 1; 1; (\rho - 1)/\rho) \tag{14a}$$
$$v_R^{\text{axial}} = \rho^{-\ell}{}_2F_1(\ell + \jmath + 1, \ell - \jmath + 1; 2(\ell + 1); \rho^{-1}), \tag{14b}$$

where for gravitational perturbations the spin $\jmath = 2$. Evidently, up to transformations of the dependent and independent variables, the equation $H^{\text{axial}}v = 0$ is the hypergeometric equation. The equation $H^{\text{polar}}v = 0$ involves an extra regular singular point, and its normal form is a particular realization of the Heun equation. Nevertheless, by exploiting certain intertwining relations between the polar and axial master functions [28], we are likewise able to express $v_{L,R}^{\text{polar}}$ in terms of the classical Gauss-hypergeometric function ${}_2F_1$. The Appendix gives further details.

To complete our analytic expressions for the Jost solutions, we still must determine C_L and C_R. Our notation for a time-dependent jump is, for example,

$$[[\Psi]](t) \equiv \lim_{\epsilon \to 0^+} [\Psi(t, r_p(t) + \epsilon) - \Psi(t, r_p(t) - \epsilon)]$$

$$= \lim_{\epsilon \to 0^+} [\Psi(t, r_p + \epsilon) - \Psi(t, r_p - \epsilon)], \qquad (15)$$

with the last equality holding for a circular orbit. As derived in Ref. [15], for a circular orbit the analytical jump determined by Eq. (1) is

$$[[\Psi_{\text{analytic}}]](t) = \frac{F(t, r_p)}{f_p}, \qquad (16)$$

where the subscript p indicates evaluation at the particle location. For trivial initial data (that is $\Psi = 0$) this jump will in general not be satisfied at $t = 0$. We find empirically that the jump in Ψ_{Jost} exactly cancels $[[\Psi_{\text{analytic}}]](0)$, while the jump in $\partial_x \Psi_{\text{Jost}}$ is zero. The system of equations used to determine our constants is therefore

$$v_R(r_p)C_R - v_L(r_p)C_L = -\frac{F(0, r_p)}{f_p} \qquad (17)$$

$$v_R'(r_p)C_R - v_L'(r_p)C_L = 0,$$

which has solution

$$C_R = -\frac{F(0, r_p)}{f_p}\left(\frac{v_L'}{v_R v_L' - v_L v_R'}\right)_p, \qquad C_L = C_R\left(\frac{v_R'}{v_L'}\right)_p. \qquad (18)$$

Recall that Ψ_{Jost} may be numerically approximated as $\Psi_{\text{impulsive}} - \Psi_{\text{smooth}}$ [cf. Equation (9)]. Figure 3 depicts the relative error $|(\Psi_{\text{Jost}} - (\Psi_{\text{impulsive}} - \Psi_{\text{smooth}}))/\Psi_{\text{Jost}}|$ for $\ell = 3$ perturbations, with Ψ_{Jost} given by (11). To generate this figure, we have used nearly the same setup as described for Fig. 2, but with the outer boundary $b = 240 + 2\log(119)$ and final time $t_F = 3100$.

C. Jost solution and radiation boundary conditions

We wish to examine the extent to which the right analytic Jost solutions $v_R^{\text{axial/polar}}$ satisfy radiation boundary conditions based on Laplace convolution [27,29], as these are boundary conditions adopted for our numerical simulations. Unfortunately, for black hole perturbations the
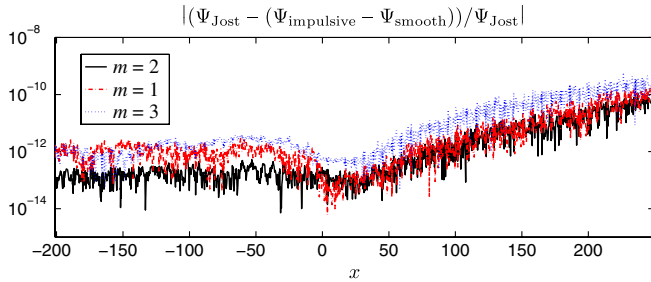

FIG. 3 (color online). Comparison between analytic and numerical Jost solutions. CPM and ZM modes, respectively, correspond to $(\ell, m) = (3, 2)$ and $(\ell, m) = (3, 1), (3, 3)$.

issue would seem difficult to address analytically. Therefore, we consider the analogous issue for the flat-space radial wave equation.

Consider a multipole solution $r^{-1}\Psi(t, r)Y_{\ell m}(\theta, \phi)$ to the ordinary flatspace $3 + 1$ wave equation, and assume the multipole is initially of compact support in radius r. Exact nonreflecting boundary conditions relative to a sufficiently large outer boundary radius b then take the form [29]

$$\left(\frac{\partial \Psi}{\partial t} + \frac{\partial \Psi}{\partial r}\right)\Big|_{r=b} = \frac{1}{b^2}\sum_{j=1}^{\ell} k_{\ell,j}\int_0^t \exp(b^{-1}k_{\ell,j}(t - t'))$$

$$\times \Psi(t', b)dt'. \qquad (19)$$

Here $\{k_{\ell,j}: j = 1, \ldots, \ell\}$ are the roots of the modified cylindrical Bessel function $K_{\ell+1/2}(x)$, also known as MacDonald's function. All $k_{\ell,j}$ lie in the left-half plane. Moreover, the scaled roots $k_{\ell,j}/(\ell + 1/2)$ accumulate on a fixed transcendental curve as ℓ grows [27,29], so the exponentials $\exp(b^{-1}k_{\ell,j}t)$ tend to decay more quickly in time $t > 0$ for larger ℓ.

For the flatspace setting at hand, the Jost solution satisfies

$$v'' - \frac{\ell(\ell + 1)}{r^2}v = 0, \qquad (20)$$

and two appropriate linearly independent solutions are the following:

$$v_L(r) = r^{\ell+1}, \qquad v_R(r) = r^{-\ell}. \qquad (21)$$

We therefore examine to what extent $v_R(r)$ satisfies (19). Straightforward calculation yields

$$\left(\frac{\partial v_R}{\partial r}\right)\Big|_{r=b} = -b^{-1}v_R(b)\sum_{j=1}^{\ell} \exp(b^{-1}k_{\ell,j}t)$$

$$+ \frac{1}{b^2}\sum_{j=1}^{\ell} k_{\ell,j}\int_0^t \exp(b^{-1}k_{\ell,j}(t - t'))$$

$$\times v_R(b)dt'. \qquad (22)$$

The function $v_R(r)$ does not satisfy the nonreflecting condition (19); however, the violation of (19) decays exponentially fast. For black hole perturbations we likewise expect that $v_R^{\text{axial/polar}}(\rho)$ violates our radiation boundary conditions only by exponentially decaying terms, and have seen some evidence of this behavior in our numerical simulations.

We have also observed persistent junk solutions when adopting the Sommerfeld condition at the outer boundary b along with impulsive start-up. We differentiate between two scenarios: the first involving a detector which is not in causal contact with the outer boundary b during the simulation, and a second with the detector located at b. For the first scenario, the static junk solution which develops and persists around the detector is precisely Ψ_{Jost}. For the

second, we also observe a persistent junk solution, but one which is distorted from Ψ_{Jost} in a boundary layer near b. Such distortion presumably arises since Ψ_{Jost} satisfies the outer Sommerfeld condition only up to an $O(r^{-\ell-1})$ error term.

III. CONSEQUENCES OF IMPULSIVE STARTING CONDITIONS

A. Inconsistent modeling of the axial sector

Axial perturbations are described by either the Cunningham-Price-Moncrief master function Ψ^{CPM} or the Regge-Wheeler master function Ψ^{RW}. Both solve the generic wave Eq. (1) with potential (10). However, the wave equations for Ψ^{CPM} and Ψ^{RW} have different distributional source terms [14,15,30]. As shown in [30], these master functions obey

$$\Psi^{\text{RW}} + \frac{1}{2}\Pi^{\text{CPM}} = 0, \qquad r \neq r_p(t), \qquad (23)$$

and we refer to this formula as the *axial consistency condition*. For circular orbits this condition becomes $\Psi^{\text{RW}} - \frac{1}{2}\partial_t\Psi^{\text{CPM}} = 0$, $r \neq r_p$. We now numerically examine the extent to which the axial consistency condition is violated when the master functions $\Psi^{\text{RW,CPM}}$ are obtained with and without smoothing.

For all experiments we again enforce Sommerfeld boundary conditions at the left physical boundary, and radiation outer boundary conditions on the right boundary. Now our smoothing parameters are $t_0 = 0$, $\tau = 100$, and $\delta = 0.05$. We compute the $(\ell, m) = (2, 1)$ metric perturbations for a particle in circular orbit initially at $(r, \phi) = (7.9456, 0)$. Other parameters (cf. Table I) are $a = -200$, $b = 30 + 2\log(14) \simeq 35.28$, $S_L = 22$, $S_R = 3$, $N = 31$, $\Delta t = 0.01$, and $t_F = 800$. We first plot $|\Psi^{\text{RW}} + \frac{1}{2}\Pi^{\text{CPM}}|$ at various times. The left panels in Fig. 4 show results with smoothing. Although the consistency condition is initially violated, the expression eventually relaxes to a small value once the dynamical junk has propagated off the domain. The right panels in Fig. 4 show the result without smoothing. Even at late times violation in the axial consistency condition is now evident. The plots in Fig. 5 depict $|\Psi^{\text{RW}} + \frac{1}{2}\Pi^{\text{CPM}}|$ recorded as a time series at $x = -200$. The plot for smooth start-up indicates that quasinormal ringing and Price decay tails characterize the late-stage dynamical junk, although this ringing is suppressed with more smoothing (e.g., with $\tau = 150$, $\delta = 0.0058$). The plot for impulsive start-up suggests that a static Jost junk solution $\Psi^{\text{RW}}_{\text{impulsive}} - \Psi^{\text{RW}}_{\text{smooth}}$ persists indefinitely (Π^{CPM} should be unaffected by a similar Jost solution in Ψ^{CPM}).

B. Contamination of waveforms

For a given (ℓ, m) multipole either read off at a finite radius or measured at null infinity through an approximate extraction, we can apply standard formulas to estimate the
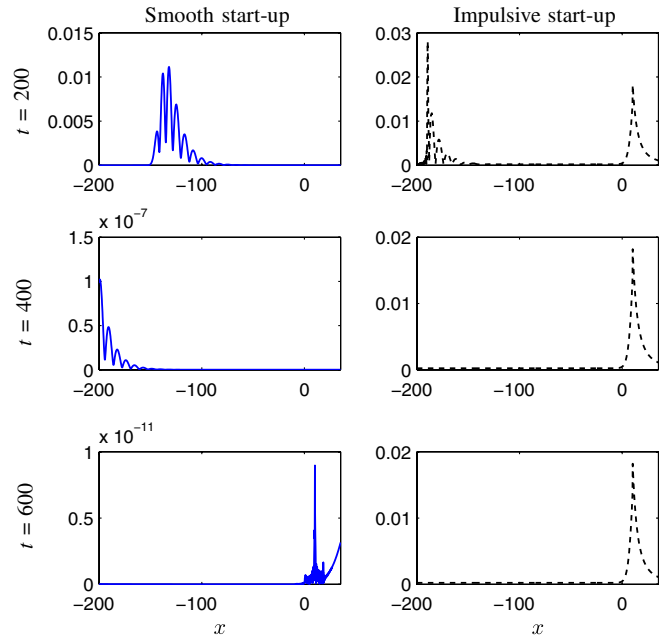

FIG. 4 (color online).   Snapshots of $|\Psi^{\text{RW}} + \frac{1}{2}\Pi^{\text{CPM}}|$ with and without smoothing. The left three panels correspond to smooth start-up and the right three to impulsive start-up. The times at the far left correspond to both sets of panels. Ψ^{RW} is of order 10^{-2} near r_p.

energy and angular momentum carried away by the gravitational waves. We continue to work with the axial perturbations, with formulas featuring only CPM and RW master functions. The luminosity expressions are the following: [14,17,30]
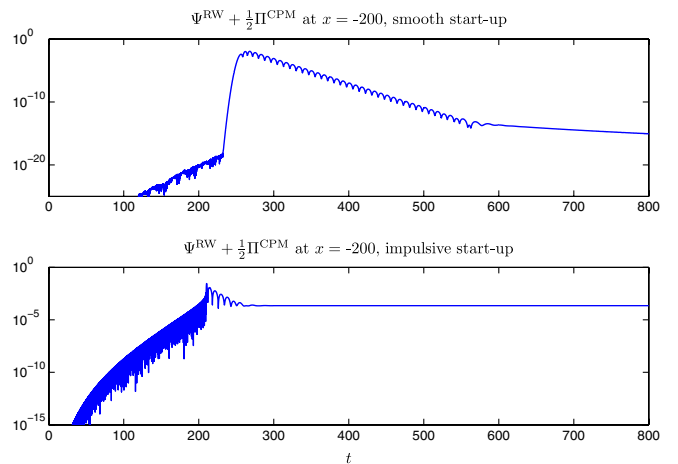

FIG. 5 (color online).   Time series at $x = -200$ for $|\Psi^{\text{RW}} + \frac{1}{2}\Pi^{\text{CPM}}|$ with and without smoothing. Ψ^{RW} is of order 10^{-4} at $x = -200$.

$$\dot{E}^{\text{CPM}}_{\ell m} = \frac{1}{64\pi} \frac{(\ell+2)!}{(\ell-2)!} |\dot{\Psi}^{\text{CPM}}_{\ell m}|^2$$

$$\dot{L}^{\text{CPM}}_{\ell m} = \frac{im}{64\pi} \frac{(\ell+2)!}{(\ell-2)!} \bar{\Psi}^{\text{CPM}}_{\ell m} \dot{\Psi}^{\text{CPM}}_{\ell m} \qquad (24a)$$

$$\dot{E}^{\text{RW}}_{\ell m} = \frac{1}{16\pi} \frac{(\ell+2)!}{(\ell-2)!} |\Psi^{\text{RW}}_{\ell m}|^2$$

$$\dot{L}^{\text{RW}}_{\ell m} = \frac{im}{16\pi} \frac{(\ell+2)!}{(\ell-2)!} \Psi^{\text{RW}}_{\ell m} \int \bar{\Psi}^{\text{RW}}_{\ell m} \, dt. \qquad (24b)$$

In the distant wave-zone we expect $\dot{E}^{\text{CPM}}_{\ell m} = \dot{E}^{\text{RW}}_{\ell m}$ and $\dot{L}^{\text{CPM}}_{\ell m} = \dot{L}^{\text{RW}}_{\ell m}$. However, Sec. III A has shown that impulsive start-up can result in violation of the axial consistency condition (23), and such violation in turn results in discrepancies between the above luminosity formulas. As seen in Sec. II B, whether simulations are based on Ψ^{CPM} or Ψ^{RW}, an impulsive start-up generates a Jost junk solution, even at long distances from the source. Although dynamical junk is also present, its effect is negligible in the wave-zone at late times.

Table II collects summed luminosities for $(\ell, m) = (2, \pm 1)$ waveforms. The top set of numbers are unaveraged and recorded at time $t_F = 2750$, while the bottom set have been averaged between $t = 2500$ and $t_F = 2500 + 4T_\phi$, where $T_\phi = 2\pi p^{3/2} \simeq 140.7246$. Other parameters (cf. Table I) are $a \simeq -190.34$, $b = 1000 + 2\log(499) \simeq 1012.43$, $S_L = 30$, $S_R = 150$, $N = 26$, and $\Delta t = 0.038$. For smoothing we use $\tau = 150$ and $\delta = 0.0058$. For circular orbits we expect $\langle \dot{Q}_{\text{smooth}} \rangle = \dot{Q}_{\text{smooth}}$, where brackets denote time averaging for a generic luminosity $\dot{Q}$. Relative errors are computed by

$$\dot{Q}_{\text{error}} = \frac{|\dot{Q}_{\text{smooth}} - \dot{Q}_{\text{impulsive}}|}{|\dot{Q}_{\text{smooth}}|}. \qquad (25)$$

For the CPM luminosities computed with smoothing, time averaging has little effect. However, it does enhance the accuracy of the RW luminosities computed with smoothing. Indeed, inspection of the bottom section of Table II shows that the CPM and RW entries in the $\dot{Q}_{\text{smooth}}$ column are in excellent agreement.

Relative to the true luminosity which would be recorded at null infinity, even the exact $\dot{E}^{\text{CPM}}$ read off at $r = 1000$ would have an $O(r^{-1})$ error, but here we have viewed the read-off value as the true one. Because $\dot{E}^{\text{CPM}}$ is unaffected by the Jost junk solution, $\dot{E}^{\text{CPM}}_{\text{error}}$ estimates error stemming from both the method (here the Chebyshev scheme) and any residual dynamical junk. The other luminosities are affected by the Jost junk solution; however, as shown in the Appendix, errors which stem from the Jost solution decay faster than $1/r$. Therefore, these errors should be smaller than the $O(r^{-1})$ errors associated with using the read-off luminosities as approximations to the ones at null infinity.

C. Self-force measurements

Over long times the influence of the metric perturbations on the particle orbit should significantly affect the gravitational waveform [31], and realistic waveform computations will therefore need to include this influence. Incorporation of self-force effects constitutes one approach towards modeling this influence. Because the metric perturbations are discontinuous at the particle, self-force calculations typically require a regularization technique. In the Regge-Wheeler gauge no regularization procedure exists for generic orbits; however, direct field-regularization [32,33] seems promising. For the restricted case of circular orbits, Detweiler has shown how to directly calculate certain gauge invariant quantities in the RW gauge without regularization [34]. Detweiler's approach obtains the energy luminosity $\dot{E}_{\text{GW}}$ and angular momentum luminosity $\dot{L}_{\text{GW}}$ associated with waves escaping to null infinity and down the black hole through local self-force calculations performed at the particle,

$$\dot{E}_p = -\frac{1}{2u^t} u^\alpha u^\beta \frac{\partial h_{\alpha\beta}}{\partial t}, \qquad \dot{L}_p = \frac{1}{2u^t} u^\alpha u^\beta \frac{\partial h_{\alpha\beta}}{\partial \phi},$$
$$(26)$$

where the perturbation $h_{\alpha\beta}$ is reconstructed from Ψ and its derivatives [35]. Equations (26) hold for each (ℓ, m) mode of the metric perturbation. For perturbations described by the CPM masterfunction and with the Regge-Wheeler gauge, the nonzero contributions (for each mode) involve

TABLE II. $\ell = 2$ luminosities recorded at $r = 1000$. Entries result from addition of $m = 1$ and $m = -1$ luminosities, and they correspond to a circular orbit with $(r, \phi) = (7.9456, 0)$ initially. $\dot{Q}_{\text{error}}$ as been computed with more precision than reported for the table entries.

$\dot{Q}$	$\dot{Q}_{\text{smooth}}$	$\dot{Q}_{\text{impulsive}}$	$\dot{Q}_{\text{error}}$
$\dot{E}^{\text{CPM}}$	$8.17530620 \times 10^{-7}$	$8.17530623 \times 10^{-7}$	3.4668×10^{-9}
$\dot{E}^{\text{RW}}$	$8.17530652 \times 10^{-7}$	$8.18248752 \times 10^{-7}$	8.7838×10^{-4}
$\dot{L}^{\text{CPM}}$	$1.83102415 \times 10^{-5} + i3.24326408 \times 10^{-14}$	$1.82972897 \times 10^{-5} - i1.28610911 \times 10^{-8}$	9.9685×10^{-4}
$\dot{L}^{\text{RW}}$	$1.83047467 \times 10^{-5} - i2.16502183 \times 10^{-8}$	$1.66825388 \times 10^{-5} + i8.14152318 \times 10^{-7}$	9.9693×10^{-2}
$\langle \dot{E}^{\text{CPM}} \rangle$	$8.17530620 \times 10^{-7}$	$8.17530620 \times 10^{-7}$	2.8376×10^{-10}
$\langle \dot{E}^{\text{RW}} \rangle$	$8.17530617 \times 10^{-7}$	$8.17531431 \times 10^{-7}$	9.9661×10^{-7}
$\langle \dot{L}^{\text{CPM}} \rangle$	$1.83102416 \times 10^{-5} - i1.40467882 \times 10^{-15}$	$1.83102416 \times 10^{-5} + i3.49294212 \times 10^{-14}$	2.0738×10^{-9}
$\langle \dot{L}^{\text{RW}} \rangle$	$1.83102415 \times 10^{-5} + i4.13269715 \times 10^{-13}$	$1.82927679 \times 10^{-5} + i7.05636411 \times 10^{-9}$	1.0292×10^{-3}

$$\frac{\partial h_{t\phi}}{\partial t} = \frac{f}{2}\left(r\frac{\partial^2\Psi}{\partial t\partial r} + \frac{\partial\Psi}{\partial t}\right)X_\phi$$
$$\frac{\partial h_{t\phi}}{\partial \phi} = \frac{f}{2}\left(r\frac{\partial\Psi}{\partial r} + \Psi\right)X_{\phi\phi}$$

(27)

in a source-free region. Here X_ϕ and $X_{\phi\phi}$ are axial vector and tensor spherical harmonics [30]. When numerically forming these expressions, we replace $\partial_t\Psi$ and $\partial_r\Psi$ by $-\Pi$ and $f^{-1}\Phi$. Only when evaluated at the particle location will $\dot{E}_p$ and $\dot{L}_p$ be related to $\dot{E}_{GW}$ and $\dot{L}_{GW}$.

We now fix $\tau = 100$ and $\delta = 0.014$ to achieve a smooth start-up, run to the final time $t_F = 800$, and pick $\Delta t = 0.005$. Other parameters are the same as those in Sec. III A. We compute $\dot{E}_p$ and $\dot{L}_p$ for $(\ell, m) = (2, \pm1)$ perturbations. Because $\dot{E}_p$ is computed with time derivatives of Ψ^{CPM}, the static Jost junk solution does not impact its measurement. We therefore expect that

$$\dot{E}_p(\Psi^{\ell m}_{\text{impulsive}}) \simeq \dot{E}_p(\Psi^{\ell m}_{\text{smooth}}). \tag{40}$$

However, an impulsive start-up appears to generate more dynamical junk at late times. Figure 6 depicts $\dot{E}_p$, recorded as a time series, for both impulsive and smooth start-ups. A separate experiment based on waveform read-off near the black hole and waveform extraction at the outer boundary determines that the energy carried away by the gravitational waves is $\dot{E}_{GW} \simeq 8.3163 \times 10^{-7}$. The relative errors in the left panel of Fig. 6 are computed as $|\dot{E}_p - \dot{E}_{GW}|/\dot{E}_{GW}$, and are limited by the accuracy of $\dot{E}_{GW}$. We therefore do not expect agreement beyond a relative error of 10^{-5}, although clearly such error will settle to a constant value. The time series for both the impulsive and smooth start-up exhibit large oscillations which persist until about $t = 400$. However, beyond $t = 400$ the impulsive start-up series shows larger oscillations.

$\dot{L}_p$ depends on both Ψ^{CPM} and its spatial derivative Φ^{CPM}, whence the Jost junk solution will impact its self-force measurement. With smoothing, the time series plot for $\dot{L}_p$ looks similar to one for $\dot{E}_p$ in Fig. 6, and is not shown. We note that our self-force $\dot{L}_p$ measurement agrees with a separate experiment which finds that the angular momentum carried away by gravitational waves is $\dot{L}_{GW} \simeq 1.8626 \times 10^{-5}$. Figure 7 shows that $\dot{L}_p$ is typically discontinuous at the particle for an impulsive start-up. Even with an impulsive start-up, the $\dot{L}_p$ measurement yields the correct value when averaged over an orbital period T_ϕ, and it is continuous across the particle (with the correct value) when the particle returns to its initial orbital angle.

These phenomena are a consequence of the axial Jost junk solution (11). For t fixed, Eq. (26) shows that $\dot{L}_p(\Psi)$ depends linearly on Ψ. Therefore, $\dot{L}_p(\Psi^{\ell m}_{\text{Jost}} + \Psi^{\ell m}_{\text{smooth}}) = \dot{L}_p(\Psi^{\ell m}_{\text{Jost}}) + \dot{L}_p(\Psi^{\ell m}_{\text{smooth}})$, so we can focus on $\dot{L}_p(\Psi^{\ell m}_{\text{Jost}})$ alone. The expressions (18) for $C_{L,R}$ are linear in $F(0, r_p)$, which is in turn proportional to the conjugate of an axial vector spherical harmonic X_ϕ [30]. Motivated by this observation, we "factor off" the conjugate, writing $\Psi^{\ell m}_{\text{Jost}} = \eta_\ell(x)\bar{X}^{\ell m}_\phi(\phi_0)$, where ϕ_0 is the particle's initial orbital angle and $\eta_\ell(x)$ is a real discontinuous function solely of x. The expression (26) for $\dot{L}_p$ involves $\partial h_{t\phi}/\partial\phi$, which by (27) is proportional to $X_{\phi\phi}$. In the equatorial plane $X^{\ell m}_{\phi\phi} = \partial_\phi X^{\ell m}_\phi = imX^{\ell m}_\phi$, and we conclude that $\dot{L}_p(\Psi^{\ell m}_{\text{Jost}}) = im\xi_\ell(x)\bar{X}^{\ell m}_\phi(\phi_0)X^{\ell m}_\phi(\phi_p(t))$, where $\xi_\ell(x)$ is a real discontinuous function solely of x. Therefore, when the particle returns to its initial position (that is, when $\phi_p(t) = \phi_0$), the value of $\dot{L}_p(\Psi^{\ell m}_{\text{Jost}})$ is pure imaginary and $\dot{L}_p(\Psi^{\ell m}_{\text{Jost}}) + \dot{L}_p(\Psi^{\ell,-m}_{\text{Jost}}) = 0$. For perturbations generated by a particle in circular orbit, we have seen that $\Psi^{\ell m}_{\text{impulsive}} \simeq \Psi^{\ell m}_{\text{Jost}} + \Psi^{\ell m}_{\text{smooth}}$ to high accuracy. Combination of this expression and the above arguments
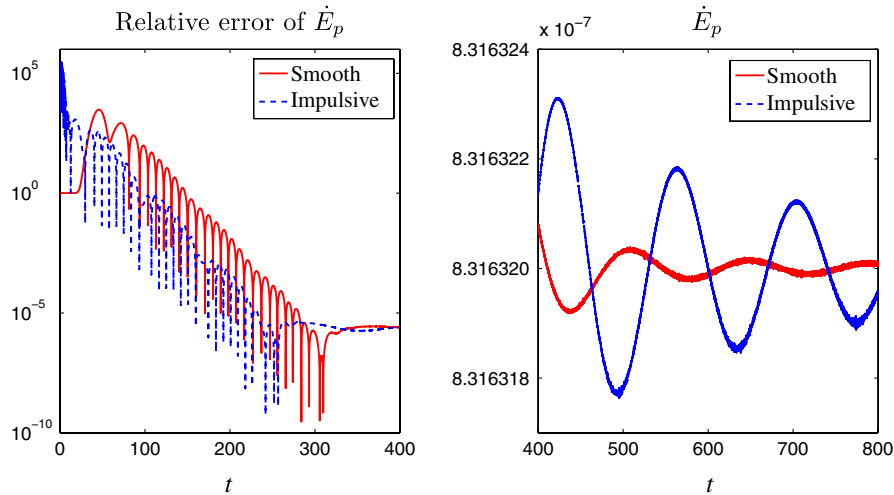

FIG. 6 (color online). $\dot{E}_p$ time series for summation of $\ell = 2$ and $m = \pm1$ modes. In the right panel the curve corresponding to impulsive start-up has the larger amplitude (due to small fluctuations this curve does not appear dashed as indicated in the legend).
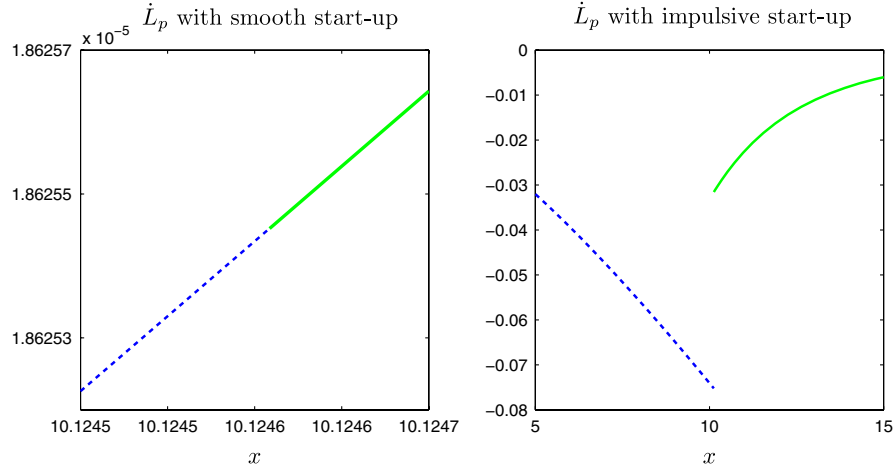
FIG. 7 (color online). $t = 800$ snapshot of real part of $\dot{L}_p$ for $\ell = 2$ and $m = 1$. The particle is located at the interface between the two subdomains.

for axial perturbations then gives

$$\sum_{|m| \leq \ell} \dot{L}_p(\Psi_{\text{impulsive}}^{\ell m}) \simeq \sum_{|m| \leq \ell} \dot{L}_p(\Psi_{\text{smooth}}^{\ell m}), \qquad (29)$$

when $\phi_p(t) = \phi_0$. Moreover, one finds $\langle \dot{L}_p(\Psi_{\text{Jost}}^{\ell m}) \rangle = 0$ for time averaging over an orbital period T_ϕ.

D. Consequences for eccentric orbits: preliminary results

This section considers a particle in the eccentric orbit described in Section IV.B.2 of [15]. In the notations of that reference the orbit's eccentricity and semilatus rectum are $(e = 0.76412402, p = 8.75456059)$, and we choose $\chi = 0.2$ and $\phi = \pi/4$ to fix the particle's initial position. We simulate the resulting $(\ell, m) = (2, 1)$ perturbation with (cf. Table I) $a = -200$, $b = 1012.43$, $S_L = 22$, $S_R = 100$, $N = 31$, $\Delta t = 0.02$, and $t_F = 3000$. We again take $\tau = 150$, $\delta = 0.0058$ as the smoothing parameters. Since $e \neq 0$, we use a coordinate transformation to keep the particle at a fixed location between subdomains (see [15] for details). Before making comparisons, we first interpolate all fields onto a uniform x–grid (tortoise coordinate) with 6063 points.

Figure 8 shows the difference between fields for smooth and impulsive start-ups. The two numerical solutions are clearly different, although for the case of eccentric orbits we have no analytical understanding of the resulting "junk solution"[2] presumably seeded by impulsive start-up. Empirically, we find that this solution satisfies

---

[2]At present, we are uncertain if the generated junk solution fulfills the formal definition of a Jost solution. Thus, in the context of eccentric orbits we simply refer to the persistent solution as the "junk solution."

$$[[\Psi_{\text{junk}}]](t) = -[[\Psi_{\text{analytic}}]](0) \qquad (30a)$$
$$[[\Phi_{\text{junk}}]](t) = 0 \qquad (30b)$$
$$[[\Pi_{\text{junk}}]](t) = 0, \qquad (30c)$$

where $[[\Psi_{\text{analytic}}]](t) = f_p(t)F(t, r_p(t))/(f_p^2(t) - \dot{r}_p^2(t))$ in terms of $f_p(t) = f(r_p(t))$. See [15] for a derivation of the analytical jump. These time-independent jump conditions are the same as for the circular orbit Ψ_{Jost} solution. With our choice of numerical parameters the axial consistency condition is satisfied to better than a 1×10^{-6} relative error throughout the entire domain for a smooth start-up. For an impulsive start-up the condition is violated to the order of
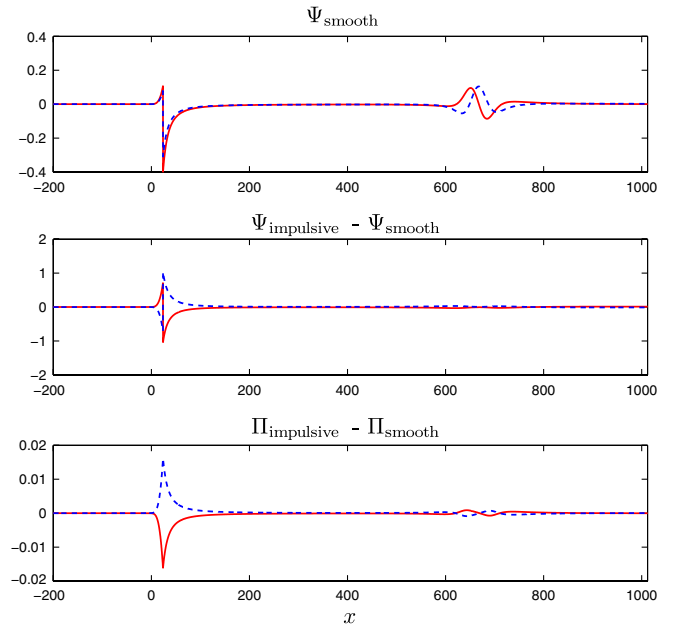

FIG. 8 (color online).   Difference between CPM fields with and without smoothing for an eccentric orbit. Here we plot both real (dashed) and imaginary (solid) parts at $t_F = 3000$.

TABLE III. $\ell = 2$ luminosities for a particle with an orbit given by ($e = 0.76412402$, $p = 8.75456059$). Entries result from the addition of $|m|$ and $-|m|$ luminosities.

$\dot{Q}$	$\dot{Q}_{\text{smooth}}$	$\dot{Q}_{\text{impulsive}}$	$\dot{Q}_{\text{error}}$
$\langle \dot{E}^{\text{ZM}}_{2,2} \rangle$	1.559917×10^{-4}	1.559484×10^{-4}	2.775789×10^{-4}
$\langle \dot{E}^{\text{CPM}}_{2,1} \rangle$	1.153983×10^{-6}	1.236758×10^{-6}	7.172983×10^{-2}
$\langle \dot{E}^{\text{RW}}_{2,1} \rangle$	1.153983×10^{-6}	1.872073×10^{-6}	6.222709×10^{-1}
$\langle \dot{E}^{\text{CPM}}_{2,1} \rangle + \langle \dot{E}^{\text{ZM}}_{2,2} \rangle$	1.571457×10^{-4}	1.571852×10^{-4}	2.512000×10^{-4}
$\text{Re}\langle \dot{L}^{\text{ZM}}_{2,2} \rangle$	2.078556×10^{-3}	2.076811×10^{-3}	8.395251×10^{-4}
$\text{Re}\langle \dot{L}^{\text{CPM}}_{2,1} \rangle$	1.441737×10^{-5}	1.537876×10^{-5}	6.668276×10^{-2}
$\text{Re}\langle \dot{L}^{\text{RW}}_{2,1} \rangle$	1.441749×10^{-5}	1.662726×10^{-5}	1.532701×10^{-1}
$\text{Re}\langle \dot{L}^{\text{CPM}}_{2,1} \rangle + \text{Re}\langle \dot{L}^{\text{ZM}}_{2,2} \rangle$	2.092973×10^{-3}	2.092190×10^{-3}	3.744004×10^{-4}

the solution itself. We conclude that, as for circular orbits, the junk solution generated by an impulsive start-up leads to an inconsistent modeling of the axial sector.

Table III collects energy and angular momentum luminosities. These luminosities have been averaged from $t = 1700$ to $t_F = 1700 + 4T_r$, where $T_r \simeq 780.6256$ is the radial period (see [15] for further details). Unlike the circular orbit case, the discrepancy between waveforms corresponding to smoothly and impulsively started fields may be larger than usual $O(1/r)$ error associated with read-off at a finite radial location rather than infinity. Moreover, the junk solution would seem determined by the initial orbital parameters. Indeed, the values $\dot{Q}_{\text{impulsive}}$ and errors quoted in our table strongly depend upon such choices.

IV. CONCLUSIONS

A number of time-domain methods exist for solving Eq. (1) as an initial boundary value problem, including those described in [9,14,17,25,26,36,37]. These methods vary in both the underlying numerical scheme (e.g., finite-difference, finite element, pseudospectral, and spectral) as well as their treatment of the distributional source terms (e.g., Gaussian representation, analytic integration, domain matching). Numerical simulation of metric perturbations may also involve other choices (e.g., gauge, number of spatial dimensions, choice of numerical variables). Moreover, similar time-domain methods exist for solving the forced Teukolsky equation describing particle-driven perturbations of the Kerr geometry (see, for example, Refs. [38–40]). For all of these methods, the issue of impulsive start-up would seem pertinent, although clearly we cannot examine each method. Nevertheless, we now attempt to provide at least partial insight into the ubiquity of static junk solutions.

As mentioned earlier, the results and observations of this paper have been independently confirmed with each of our two numerical methods: the nodal Legendre dG and Chebyshev schemes. However, as these schemes are rather similar, we now briefly consider a finite-difference scheme for solving (3), based on fourth, sixth, and eighth order stencils for the spatial derivatives. To stabilize sixth and

eighth order stencils, we have followed Ref. [41]. Furthermore, we replace the Dirac delta functions in (3) by narrow Gaussians. Precisely, for $\sigma = 0.1$ we make the replacement

$$J(x, t)\delta(x - x_p) \rightarrow J(x, t)\frac{1}{\sqrt{2\pi}\sigma} \exp\left(-\frac{(x - x_p)^2}{2\sigma^2}\right) \quad (31)$$

for both the J_1 and J_2 terms in (3). Analytic expressions for J_1 and J_2 are readily computed with Eq. (28) from Ref. [15]. With essentially the same experimental set-up described in Sec. II B, we repeat that experiment using 4000 points and sixth-order spatial differences. The results, shown in Fig. 9, clearly indicate the presence of a static "Jost junk" solution. A larger choice for σ gives rise to a rounder transition near the particle. However, the following shows that such contamination is not a generic feature. For circular orbits, our system (3) becomes
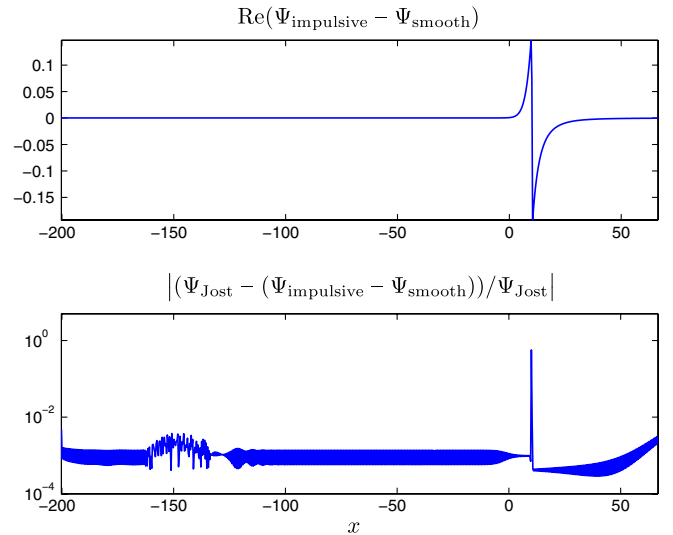

FIG. 9 (color online).   Difference between smoothly and impulsively started fields using a finite-difference method. As in Sec. II B, we consider Ψ^{CPM} for $\ell = 3$ and $m = 2$. The bottom plot depicts the relative error between the numerical and analytical Jost solutions.

$$\partial_t \Psi = -\Pi, \qquad \partial_t \Pi = -\partial_x \Phi + V(r)\Psi + J_1 \delta(x - x_p)$$

$$\partial_t \Phi = -\partial_x \Pi + J_2 \delta(x - x_p), \tag{32}$$

where the time-dependent jump factors are $J_1 = [[\Psi_x]]$ and $J_2 = -[[\Psi_t]]$. We introduce a variable $\tilde{\Phi}$ obeying

$$\Phi = \tilde{\Phi} - [[\Psi]]\delta(x - x_p), \tag{33}$$

so that the system formally becomes

$$\partial_t \Psi = -\Pi$$

$$\partial_t \Pi = -\partial_x \tilde{\Phi} + V(r)\Psi + J_1 \delta(x - x_p) + J_3 \delta'(x - x_p)$$

$$\partial_t \tilde{\Phi} = -\partial_x \Pi, \tag{34}$$

where $J_3 = [[\Psi]] = F(t, r_p)/f_p$. If we now replace the δ, δ' terms in the new system by appropriate Gaussians, *then we do not observe a persistent Jost junk solution* when trivial initial conditions are supplied.

Persistent junk solutions arise from the combination of inconsistent initial data and the distributional forcing terms which define the EMRB model. In particular, we observe that development of a Jost junk solution depends on how the distributional forcing is treated rather than the underlying numerical method. Therefore, whether or not they contaminate simulations should be considered on a case-by-case basis. Domain matching approaches which enforce jump conditions without approximation (considered in this paper) exhibit a Jost junk solution in the absence of smooth start-up. With first-order variables such approaches correspond to system (32) rather than (34). Treatment of system (34) with Gaussian representations for δ, δ' exhibits no persistent junk solution, although such an approach necessarily introduces large method error relative to the exact distributional model and features variables with δ-like behavior near the particle (Gaussian peak). The issue of a static junk solution for schemes which discretize the second-order Eq. (1) deserves further consideration, although, if present, then the particular Jost junk solution observed in this paper would likely be of relevance.[3]

We have shown that impulsive starting conditions are inadequate for time-domain modeling of extreme mass ratio binaries. Such conditions result in more dynamical junk, evident in self-force calculations, and potentially a static Jost junk solution which persists indefinitely. Although each effect is small compared to the physical solution, such systematic errors will corrupt studies which require high accuracy. For example, computation of waveforms accurate to second order in the mass ratio requires reconstruction of the first-order perturbations. Since these

___

[3] For a static solution to have gone unnoticed, it would seem reasonable to expect decay as either $r \to 2M^+$ or $r \to \infty$. Such solutions will necessarily be discontinuous, and presumably such discontinuities could only "hide" at the particle, requirements that fix the form of the static solution up to the constants C_L and C_R introduced in Sec. II B.

first-order terms act as sources for the wave equations describing the second-order master functions, the presence of a Jost junk solution will affect second-order waveforms. Circular orbits far from the massive central object (of potential relevance for the quasicircular phase of inspiral) are similarly impacted by the Jost junk solution. Equation (18) indicates that the magnitude of a polar-mode static junk solutions does not decay as r_p becomes large (compare with Eqs. (C5a) and (C6e) from [15]). However, such decay is present in the axial case (compare with (C8a) and (C9c) of [15]). When studying eccentric orbits, errors arising from the persistent junk solution appear to corrupt studies requiring even modest accuracy. Minimization of dynamical and Jost junk by smoothing the source terms during start-up will improve waveform templates and self-force techniques with minimal computational and human effort.

APPENDIX: TIME-INDEPENDENT MASTER EQUATIONS

1. Regge-Wheeler equation

Subject to the *Ansatz* that the solution v is time-independent and in terms of the dimensionless variable $\rho = (2M)^{-1} r$, the homogeneous Regge-Wheeler equation is [24]

$$-\left(1 - \frac{1}{\rho}\right)v'' - \frac{1}{\rho^2}v' + \left[\frac{\ell(\ell + 1)}{\rho^2} + \frac{\kappa}{\rho^3}\right]v = 0, \tag{A1}$$

where $\kappa = 1 - \jmath 2$ in terms of the spin $\jmath = 0, 1, 2$. For gravitational perturbations $\jmath = 2$, but we leave $\jmath$ unspecified for the time being. Expressing the equation in the form

$$v'' + P(\rho)v' + Q(\rho)v = 0, \qquad P(\rho) = \frac{1}{\rho(\rho - 1)}$$

$$Q(\rho) = -\frac{\ell(\ell + 1)\rho + \kappa}{\rho^2(\rho - 1)}, \tag{A2}$$

we find that it has regular singular points at 0, 1, and ∞, as well as the associated Riemann-Papperitz symbol [42]

$$v = P\left\{\begin{matrix} 0 & 1 & \infty \\ 1 + \jmath & 0 & -(\ell + 1) \\ 1 - \jmath & 0 & \ell \end{matrix} \; ; \rho \right\}. \tag{A3}$$

To obtain the standard normal form, we let $v = \rho^{1+\jmath}u$, so

that

$$u = P\left\{\begin{matrix} 0 & 1 & \infty \\ 0 & 0 & -\ell + J \\ -2J & 0 & \ell + J + 1 \end{matrix} \quad ; \rho\right\}, \quad (A4)$$

where u satisfies the hypergeometric equation

$$\rho(1 - \rho)u'' + [c - (a + b + 1)\rho]u' - abu = 0, \quad (A5)$$

with $a = -\ell + J$, $b = \ell + J + 1$, and $c = 1 + 2J$. As one of the two linearly independent solutions based at $\rho = \infty$ (chosen to be the second), we may take

$$u_2(\rho) = \rho^{-\ell - J - 1} {}_2F_1(\ell + J + 1, \ell - J + 1; 2(\ell + 1); \rho^{-1}). \quad (A6)$$

Expressed in terms of the original dependent variable, $v_2 = \rho^{1+J} u_2$, this solution is our axial/right solution $v_2(\rho) = v_R^{\text{axial}}(\rho)$ given in (14b). To obtain series solutions based at 1 which are nevertheless valid on $(1, \infty)$, we follow Leaver [43] and consider the transformation $\eta = (\rho - 1)/\rho$. Then with $w(\eta) = v(1/(1 - \eta))$, we get

$$w'' + \mathcal{P}(\eta)w' + \mathcal{Q}(\eta)w = 0, \qquad \mathcal{P}(\eta) = \frac{1 - 3\eta}{\eta(1 - \eta)}$$

$$\mathcal{Q}(\eta) = -\frac{\ell(\ell + 1) + \kappa(1 - \eta)}{\eta(1 - \eta)^2}, \quad (A7)$$

which has the P-symbol

$$w = P\left\{\begin{matrix} 0 & 1 & \infty \\ 0 & -(\ell + 1) & 1 + J \\ 0 & \ell & 1 - J \end{matrix} \quad ; \eta\right\}. \quad (A8)$$

Now let $w = (\eta - 1)^\ell y$ so that

$$y = P\left\{\begin{matrix} 0 & 1 & \infty \\ 0 & 0 & 1 + \ell + J \\ 0 & -(2\ell + 1) & 1 + \ell - J \end{matrix} \quad ; \eta\right\} \quad (A9)$$

solves

$$\eta(1 - \eta)y'' + [C - (A + B + 1)\eta]y' - ABy = 0, \quad (A10)$$

with $A = \ell - J + 1$, $B = \ell + J + 1$, and $C = 1$. Therefore, we choose $v_1(\rho) = v_L^{\text{axial}}(\rho)$ given in (14a) as both a first linearly independent solution and the axial/left one of interest.

2. Zerilli equation

In dimensionless form, the time-independent Zerilli equation is

$$-\left(1 - \frac{1}{\rho}\right)v'' - \frac{1}{\rho^2}v'$$

$$+ \left[\frac{8n^2(n + 1)\rho^3 + 12n^2\rho^2 + 18n\rho + 9}{\rho^3(2n\rho + 3)^2}\right]v = 0, \quad (A11)$$

again where $n = \frac{1}{2}(\ell - 1)(\ell + 2)$. In standard form, the equation is

$$v'' + P(\rho)v' + Q(\rho)v = 0, \qquad P(\rho) = \frac{1}{\rho(\rho - 1)}$$

$$Q(\rho) = -\left[\frac{8n^2(n + 1)\rho^3 + 12n^2\rho^2 + 18n\rho + 9}{\rho^2(\rho - 1)(2n\rho + 3)^2}\right]. \quad (A12)$$

This equation has regular singular points at 0, 1, ∞, and $-3/(2n)$, with the following associated pairs of indicial exponents: $\{1, 1\}$, $\{0, 0\}$, $\{\ell, -(\ell + 1)\}$, $\{2, -1\}$. The general second-order homogeneous ODE with regular singular points at z_0, z_1, z_2, and ∞ has the form $y'' + R(z)y' + S(z)y = 0$, with

$$R(z) = \frac{A_0}{z - z_0} + \frac{A_1}{z - z_1} + \frac{A_2}{z - z_2}$$

$$S(z) = \frac{B_0}{(z - z_0)^2} + \frac{B_1}{(z - z_1)^2} + \frac{B_2}{(z - z_2)^2} + \frac{C_0}{z - z_0}$$

$$+ \frac{C_1}{z - z_1} + \frac{C_2}{z - z_2}, \quad (A13)$$

where the A_i, B_i, and C_i are all constants subject to $C_0 + C_1 + C_2 = 0$ and the requirement that for each $i = 0, 1, 2$ at least one member of the triple A_i, B_i, and C_i must be nonzero (for otherwise z_i would be a ordinary point). By expressing all constants A_i, B_i, C_i except C_0 in terms of the indicial exponents $\{\{\lambda_k, \lambda_k'\}: k = 0, 1, 2, \infty\}$, we find

$$R(z) = \frac{1 - \lambda_0 - \lambda_0'}{z - z_0} + \frac{1 - \lambda_1 - \lambda_1'}{z - z_1} + \frac{1 - \lambda_2 - \lambda_2'}{z - z_2}$$

$$S(z) = \frac{\lambda_0\lambda_0'}{(z - z_0)^2} + \frac{\lambda_1\lambda_1'}{(z - z_1)^2} + \frac{\lambda_2\lambda_2'}{(z - z_2)^2}$$

$$+ \frac{\lambda_\infty\lambda_\infty' - \lambda_0\lambda_0' - \lambda_1\lambda_1' - \lambda_2\lambda_2'}{(z - z_1)(z - z_2)}$$

$$+ \frac{C_0(z_0 - z_1)(z_0 - z_2)}{(z - z_0)(z - z_1)(z - z_2)}. \quad (A14)$$

Here $-C_0$ is the *accessory parameter* [44], and the generalized Riemann scheme [44] associated with the equation is

$$\begin{bmatrix} 1 & 1 & 1 & 1 & \\ z_0 & z_1 & z_2 & \infty & ; z \\ \lambda_0 & \lambda_1 & \lambda_2 & \lambda_\infty & ; -C_0 \\ \lambda_0' & \lambda_1' & \lambda_2' & \lambda_\infty' & \end{bmatrix}. \quad (A15)$$

The notation is similar to the P-symbol, but also indicates

the type of singular points in the first row (regular singular points are indicated by a 1). We find the scheme

$$
\begin{bmatrix}
1 & 1 & 1 & 1 & \\
0 & 1 & -3/(2n) & \infty & ;\rho \\
1 & 0 & 2 & -(\ell+1) & ;0 \\
1 & 0 & -1 & \ell &
\end{bmatrix},
\qquad (A16)
$$

for the specific case of the time-independent Zerilli equation (A11).

Upon transforming the ODE specified by (A14) to normal form, we find the new accessory parameter

$$
\begin{aligned}
q = -C_0 &+ \frac{\lambda_0(\lambda_1' - 1) + \lambda_1(\lambda_0' - 1)}{z_0 - z_1} \\
&+ \frac{\lambda_0(\lambda_2' - 1) + \lambda_2(\lambda_0' - 1)}{z_0 - z_2},
\end{aligned}
\qquad (A17)
$$

as well as the transformed scheme

$$
\begin{bmatrix}
1 & 1 & 1 & 1 & \\
z_0 & z_1 & z_2 & \infty & ;z \\
0 & 0 & 0 & \lambda_\infty + \lambda_0 + \lambda_1 + \lambda_2 & ;q \\
\lambda_0' - \lambda_0 & \lambda_1' - \lambda_1 & \lambda_2' - \lambda_2 & \lambda_\infty' + \lambda_0 + \lambda_1 + \lambda_2 &
\end{bmatrix}.
\qquad (A18)
$$

With the assumptions $z_0 = 0$ and $z_1 = 1$, this scheme corresponds to the Heun equation $G'' + P(z)G' + Q(z)G = 0$ in normal form, where

$$
\begin{aligned}
P(z) &= \frac{c}{z} + \frac{d}{z-1} + \frac{1+a+b-c-d}{z-z_2} \\
Q(z) &= \frac{ab}{(z-1)(z-z_2)} - \frac{qz_2}{z(z-1)(z-z_2)}.
\end{aligned}
\qquad (A19)
$$

Here the transformed scheme

$$
\begin{bmatrix}
1 & 1 & 1 & 1 & \\
0 & 1 & z_2 & \infty & ;z \\
0 & 0 & 0 & a & ;q \\
1-c & 1-d & c+d-a-b & b &
\end{bmatrix}
\qquad (A20)
$$

is expressed in terms of the constants a, b, c, and d which may be related to the above exponent pairs $\{\lambda_k, \lambda_k'\}$. The normal form of (A11) then has the scheme

$$
\begin{bmatrix}
1 & 1 & 1 & 1 & \\
0 & 1 & -3/(2n) & \infty & ;\rho \\
0 & 0 & 0 & 2-\ell & ;1-4n/3 \\
0 & 0 & -3 & \ell+3 &
\end{bmatrix}.
\qquad (A21)
$$

While the preceding analysis both addresses the structure of the time-independent Zerilli equation and reveals the asymptotic behavior of the solutions near any given singular point, it does not provide concrete analytical expressions for the solutions $v_{L,R}^{\text{polar}}$ considered in the main text. To obtain such expressions, we use the intertwining operators [28]

$$
D_\pm = \left(1 - \frac{1}{\rho}\right)\frac{d}{d\rho} \pm \left[\frac{2}{3}n(n+1) + \frac{3(\rho-1)}{\rho^2(3+2n\rho)}\right].
\qquad (A22)
$$

Using our earlier solutions $v_{L,R}^{\text{axial}}(\rho)$ to the time-independent Regge-Wheeler equation, we then get corresponding solutions $v_{L,R}^{\text{polar}}(\rho) \equiv D_+ v_{L,R}^{\text{axial}}(\rho)$ to (A11) by direct application of D_+ and the identity

$$
\frac{d}{dz}\,{}_2F_1(a,b;c;z) = \frac{ab}{c}\,{}_2F_1(a+1,b+1;c+1;z).
\qquad (A23)
$$

Therefore, we have also expressed the relevant polar solutions in terms of the Gauss-hypergeometric function ${}_2F_1$. The analysis above then shows that we are likewise able to express solutions to a particular instance of the Heun equation in terms of hypergeometric functions.

---

[1] T. Damour, Phys. Rev. D **81**, 024017 (2010).
[2] N. Yunes, A. Buonanno, S. A. Hughes, M. C. Miller, Y. Pan, Phys. Rev. Lett. **104**, 091102 (2010).
[3] A. Nagar, T. Damour, and A. Tartaglia, Classical Quantum Gravity **24**, S109 (2007).
[4] C. R. Galley and B. L. Hu, Phys. Rev. D **79**, 064002 (2009).
[5] C. R. Galley and M. Tiglio, Phys. Rev. D **79**, 124027 (2009).
[6] L. Blanchet, S. Detweiler, A. Le Tiec, B. F. Whiting, Phys. Rev. D **81**, 064004 (2010).
[7] S. Detweiler, arXiv:0908.4363.
[8] S. Detweiler, Classical Quantum Gravity **22**, S681 (2005).
[9] L. Barack, Classical Quantum Gravity **26**, 213001 (2009).
[10] T. Tanaka, Prog. Theor. Phys. Suppl. **163**, 120 (2006).
[11] L. Barack and N. Sago, Phys. Rev. D **75**, 064021 (2007).
[12] L. Barack, Y. Mino, H. Nakano, A. Ori, and M. Sasaki, Phys. Rev. Lett. **88**, 091101 (2002).
[13] N. Sago and L. Barack (unpublished); Calculation of the gravitational self-force in Schwarzschild spacetime, presentation given by N. Sago at the 12th Capra Meeting on Radiation Reaction, www.astro.indiana.edu/~jthorn/capra12/.
[14] K. Martel, Phys. Rev. D **69**, 044025 (2004).

[15] S.E. Field, J.S. Hesthaven, and S.R. Lau, Classical Quantum Gravity **26**, 165010 (2009).

[16] S. Chandrasekhar, *The Mathematical Theory of Black Holes* (Oxford University Press, Oxford, 2000).

[17] C.F. Sopuerta and P. Laguna, Phys. Rev. D **73**, 044028 (2006).

[18] C. Cutler, D. Kennefick, and E. Poisson, Phys. Rev. D **50**, 3816 (1994).

[19] K. Martel and E. Poisson, Phys. Rev. D **66**, 084001 (2002).

[20] R.H. Price and L.M. Burko, Phys. Rev. D **70**, 084039 (2004).

[21] M. Campanelli and C.O. Lousto, Phys. Rev. D **58**, 024015 (1998).

[22] M. Campanelli, W. Krivan, and C.O. Lousto, Phys. Rev. D **58**, 024016 (1998).

[23] A. Zenginoglu, Classical Quantum Gravity **27**, 045015 (2010).

[24] R. Donninger, W. Schlag, and A. Soffer, arXiv:0908.4292.

[25] P. Cañizares and C.F. Sopuerta, J. Phys. Conf. Ser. **154**, 012053 (2009).

[26] P. Cañizares and C.F. Sopuerta, Phys. Rev. D **79**, 084020 (2009).

[27] S.R. Lau, J. Math. Phys. (N.Y.) **46**, 102503 (2005).

[28] A. Anderson and R.H. Price, Phys. Rev. D **43**, 3147 (1991).

[29] B. Alpert, L. Greengard, and T. Hagstrom, SIAM J. Numer. Anal. **37**, 1138 (2000).

[30] K. Martel and E. Poisson, Phys. Rev. D **71**, 104003 (2005). Expanded version available as arXiv:gr-gc/0502028.

[31] L.M. Burko, Phys. Rev. D **67**, 084001 (2003).

[32] I. Vega and S. Detweiler, Phys. Rev. D **77**, 084008 (2008).

[33] I. Vega, P. Diener, W. Tichy, and S. Detweiler, Phys. Rev. D **80**, 084021 (2009).

[34] S. Detweiler, Phys. Rev. D **77**, 124026 (2008).

[35] C.O. Lousto, Classical Quantum Gravity **22**, S569 (2005).

[36] C.O. Lousto, Classical Quantum Gravity **22**, S543 (2005).

[37] J.-H. Jung, G. Khanna, and I. Nagle, Int. J. Mod. Phys. C **20**, 1827 (2009).

[38] R. López-Alemán, G. Khanna, J. Pullin, Classical Quantum Gravity **20**, 3259 (2003).

[39] P.A. Sundararajan, G. Khanna, and S.A. Hughes, Phys. Rev. D **76**, 104005 (2007).

[40] P.A. Sundararajan, G. Khanna, S.A. Hughes, and S. Drasco, Phys. Rev. D **78**, 024022 (2008).

[41] G. Hagstrom and T. Hagstrom, J. Comput. Phys. **223**, 316 (2007).

[42] J. Mathews and R.L. Walker, *Methods of Mathematical Physics* (W.A. Benjamin, Inc., New York, 1965).

[43] E.W. Leaver, J. Math. Phys. (N.Y.) **27**, 1238 (1986).

[44] S.Y. Slavyanov and W. Lay, *Special Functions: A Unified Theory Based on Singularities* (Oxford University Press, Oxford, 2000).